ACS OMEGA

Open Access

http://pubs.acs.org/journal/acsodf

Article

FeN_4-Embedded Graphene as a Highly Sensitive and Selective Single-Atom Sensor for Reaction Intermediates of Electrochemical CO_2 Reduction

Yuqi Cai, Xiaocheng Zhou,* Yu Wang, and Yafei Li*

Cite This: *ACS Omega* 2024, 9, 32167−32174

Read Online

ACCESS | Metrics & More | Article Recommendations | Supporting Information

ABSTRACT: Exploring effective ways to detect intermediates during the electrochemical CO_2 reduction reaction (CO_2RR) process is pivotal for understanding reaction pathways and underlying mechanisms. Recently, two-dimensional FeN_4-embedded graphene has received increasing attention as a promising catalyst for CO_2RR. Here, by means of density functional theory computations combined with the non-equilibrium Green's function (NEGF) method, we proposed a detection device to evaluate the performance of FeN_4-embedded graphene in intermediates detection during the CO_2RR process. Our results reveal that the four key intermediates, including *COOH, *OCHO, *CHO, and *COH, can be chemisorbed on FeN_4-embedded graphene with high adsorption energies and appropriate charge transfer. The computed current−voltage (I−V) characteristics and transmission spectra suggest that the adsorption of these intermediates induces significant type-dependent changes in currents and transmission coefficients of FeN_4-embedded graphene. Remarkably, the FeN_4-embedded graphene is more sensitive to *COOH and *COH than to *OCHO and *CHO within the entire bias window. Consequently, our theoretical study indicates that the FeN_4-embedded graphene can effectively detect the key intermediates during the CO_2RR process, providing a practical scheme for identifying catalytic reaction pathways and elucidating underlying reaction mechanisms.

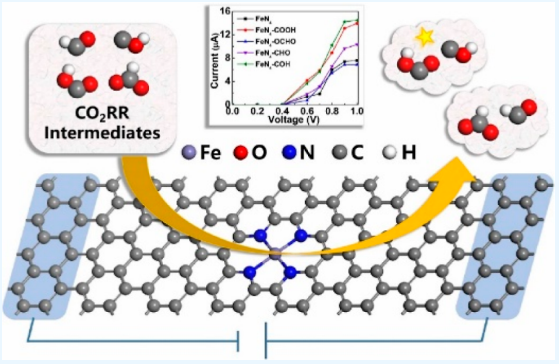

1. INTRODUCTION

The large-scale use of fossil energy has emitted a large amount of carbon dioxide (CO_2), causing many environmental problems, such as air pollution and global warming.[1,2] The electrochemical reduction of CO_2 to high-value chemicals by the electrochemical reduction method provides a promising way for the conversion and storage of electrical energy generated by renewable energy sources and also contributes to the mitigation of environmental problems.[3−5] It is worth noting that the electrochemical CO_2 reduction reaction (CO_2RR) is a multi-electron reaction involving complex intermediates, numerous products, and complicated reaction pathways.[6,7] Therefore, real-time detection of the reaction intermediates becomes particularly significant for understanding the reaction mechanism and further optimizing CO_2 reduction catalytic performance.

Experimentally, various detection methods can be used to detect intermediates and reaction products in the CO_2RR process.[8,9] For example, in situ Raman spectroscopy and in situ Fourier transform infrared spectroscopy have been used to monitor the intermediates in real time and reveal the reaction pathways and mechanisms of CO_2RR.[10,11] As another example, in situ mass spectrometry can be conducted to detect the transient intermediate products and gain insight into the local reaction environment during the reaction process.[12,13] In addition to in situ detection, Clark and Bell used cyclic voltammetry to determine the abundance of CO_2RR products and inferred catalytic reaction pathways and products.[14] Notably, CO_2 reduction is a multi-path reaction with rapid catalytic reaction rates, wherein the catalysts undergo changes, and the intermediates are complex and diverse. Therefore, it is challenging for conventional characterization techniques to monitor the catalyst evolution and capture the transient intermediate products. While valuable, in situ characterization techniques are also limited in catalytic systems, reaction conditions, operating environment, and detection accuracy. Thus, it is desirable to develop efficient detection methods based on simple catalysts to monitor the evolution of intermediates and reveal the mechanism of CO_2RR processes.

In recent decades, two-dimensional (2D) materials have been extensively explored for electrochemical catalysis and

Received: May 10, 2024
Revised: June 24, 2024
Accepted: July 1, 2024
Published: July 9, 2024

sensing devices due to their large specific surface area, high carrier mobility, and adjustable electronic structures.[15−18] The adsorption of molecules on 2D materials modifies the local coordination environment of the surface and induces changes in the electronic properties of the systems, such as charge distribution and density of states (DOS). These modifications subsequently result in changes in electronic transport properties, which are essential to nanoelectronics detection devices.[19,20] For instance, boron nitride (BN), transition metal dichalcogenides like MoS_2 and WS_2, MXene, silicene, phosphorene, and borophene have been utilized for gas molecule detection.[21−26] In particular, incorporating metal atoms into 2D materials can enhance the sensitivity and selectivity of detection devices due to the enhancement of interaction between the substrate and molecules. Cho et al. reported that palladium and aluminum-decorated graphene showed better gas-sensing properties than pure graphene.[27]

Recently, carbon materials doped with transition metal and nitrogen (TMN_x) have emerged as promising catalysts for CO_2RR due to their unique coordination environment, maximum atom efficiency, isolated and well-defined active sites, and excellent electrical conductivity. Due to the unique structures, these TMN_x-embedded carbon materials exhibit outstanding catalytic performance and selectivity.[28−30] In addition, several measures, such as changing transition metal atoms and N-coordination structures, have been taken to improve their CO_2RR performance.[31] In particular, FeN_4-embedded graphene has been identified as one of the most promising candidates for CO_2RR. Li et al. revealed that FeN_4-embedded graphene possessed excellent activity for CO production with a Faraday efficiency of approximately 93%.[32]

Herein, for the first time, we systematically investigated the performance of FeN_4-embedded graphene for detecting CO_2RR intermediates by density functional theory (DFT) and non-equilibrium Green's function (NEGF) calculations. We explored the adsorption energies of intermediates and the charge transfer between intermediates and substrates. The results demonstrate that the adsorption of intermediates significantly affects the electronic properties of the system. Furthermore, we calculated the system's current−voltage (I−V) characteristics and transmission spectra, which could effectively distinguish different intermediates. This study will help clarify and promote the revelation of the process and mechanism of CO_2RR.

2. COMPUTATIONAL DETAILS

Based on DFT, structure relaxation and electronic structure calculations were performed using the Vienna Ab initio Simulation Package (VASP).[33] The generalized gradient approximation with the Perdew−Burke−Ernzerhof (PBE) function was used to describe the exchange−correlation function.[34] A 1 × 2 × 1 k-mesh was used for Brillouin zone sampling, and the cutoff energy was set to be 400 eV. All structures were optimized using a force convergence standard of less than 0.07 eV/Å and an energy convergence standard of 5×10^{-5} eV. The strong correlation was taken into consideration via the PBE + U method. The effective Hubbard-U parameter (U_{eff}) for Fe was set to be 2.0 eV (Table S1). A vacuum of 20 Å was used in the z direction to prevent the interaction between two adjacent FeN_4-embedded graphene layers. The DFT-D3 method was applied to describe the vdW interactions between the intermediates and the FeN_4-embedded graphene. The Poisson−Boltzmann implicit solvation model was applied to describe the solvation effects.[35,36] We introduced the adsorption energy E_{ads} to evaluate the stability of intermediate adsorption on FeN_4-embedded graphene, which is defined as

$$E_{ads} = E_{FeN_4\text{-IM}} - E_{FeN_4} - E_{IM} \quad (1)$$

where $E_{FeN_4\text{-IM}}$, E_{FeN_4} and E_{IM} are the energies of the FeN_4-embedded graphene with adsorbed intermediates, the free FeN_4-embedded graphene and the isolated intermediate, respectively. A negative value of E_{ads} signifies an exothermic process, indicating the stable adsorption of the intermediate on FeN_4-embedded graphene.

We further designed the device based on FeN_4-embedded graphene for intermediate detection, and calculated the transport properties and sensing sensitivity. The transport properties of the device were calculated using the *NANO-DCAL* package,[37] in which the device simulations were performed by combining the non-equilibrium Green's function with DFT in real space. For the real space grid, we set a 3000 eV energy cutoff, and the convergence criterion for both the Hamiltonian and density matrix were set to 10^{-4} eV. The center region and the electrode were sampled using the k-point meshes of 1 × 3 × 1 and 100 × 3 × 1, respectively. The electrical current $I(V_b)$ under the applied bias V_b is calculated by the following equation[38]

$$I(V_b) = \frac{2e}{h}\int_{\mu_R}^{\mu_L} T(E, V_b)[f(E-\mu_L) - f(E-\mu_R)]dE \quad (2)$$

where $T(E,V_b)$ is the transmission coefficient of energy (E) at the bias V_b. $f(E-\mu_L)$ and $f(E-\mu_R)$ are the Fermi−Dirac distribution functions for the electrons in the left and right electrodes, respectively. $\mu_{R/L}$ is the chemical potential of the left/right electrode, and $\mu_L - \mu_R = V_b$. The Landauer−Büttiker formula is used to calculate the probability of incoming electrons transferred from one electrode to another with the specific energy (E) as follows

$$T(E, V_b) = \frac{e^2}{h} Tr[\Gamma_L(E) G_C(E) \Gamma_R(E) G_C^{\dagger}(E)] \quad (3)$$

where $\Gamma_{L/R}(E)$ is the coupling matrix of the L/R electrode. And $G_C(E)$ and $G_C^{\dagger}(E)$ are the retarded and advanced Green's functions, respectively.[39,40]

3. RESULTS AND DISCUSSION

3.1. Adsorption Behaviors of the Intermediates on FeN_4-Embedded Graphene. We first optimized the structure of a 4 × 4 × 1 graphene supercell with embedded FeN_4 moiety. As shown in Figure 1a, the calculated lattice parameters are 16.91 Å × 9.88 Å, with an average Fe−N bond length of about 1.88 Å, which agrees well with previous studies.[41,42] Then, we delved into the adsorption behaviors of the intermediates on FeN_4-embedded graphene. Before this, it is necessary to contemplate the possible CO_2 reduction pathways. The electrochemical reduction of CO_2 is a multiple proton-coupled electron transfer (PCET) process with various of valuable products. The protonation of CO_2 produces two competing intermediates, *COOH and *OCHO, which can be further reduced upon the transfer of the second proton/electron pair. The *COOH intermediate can be reduced to CO, while the *OCHO intermediate can be reduced to HCOOH. After that, the CO product may undergo the

https://doi.org/10.1021/acsomega.4c04465
ACS Omega 2024, 9, 32167−32174

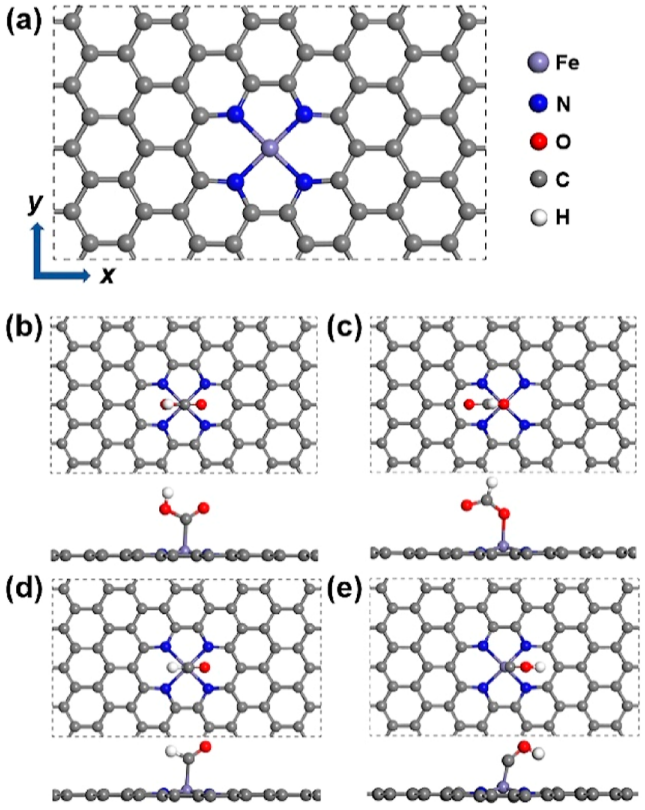

Figure 1. (a) Top view of the optimized atomic structure of 2D FeN_4-embedded graphene. Top and side views of (b) *COOH, (c) *OCHO, (d) *CHO, and (e) *COH intermediates adsorbed on FeN_4-embedded graphene.

following protonation reaction and produce *CHO or *COH intermediates, which are crucial for CH_4 or CH_3OH production. Therefore, we selected *COOH and *OCHO as the first detection group and *CHO and *COH as the second detection group. All possible adsorption configurations and orientations were considered, and Figure 1b−e present the top and side views of the most energetically favorable adsorption configurations. Notably, the optimal adsorption sites for all four intermediates are situated atop the Fe atom in the armchair direction.

As shown in Table 1, after adsorbing on FeN_4-embedded graphene, the optimized shortest distances between *COOH, *OCHO, *CHO, and *COH intermediates and Fe atom are 1.91, 1.94, 1.89, and 1.70 Å, respectively. These distances suggest the formation of a chemical bond (C−Fe or O−Fe) with the Fe atom. The calculated adsorption energies for the *COOH, *OCHO, *CHO, and *COH intermediates on FeN_4-embedded graphene are −2.25, −2.36, −2.20, and −2.68 eV, respectively, further confirming the strong interactions between them. The effects of material size and solvation effect were also considered. We calculated the adsorption energies of the intermediates using larger 5 × 5 × 1 and 6 × 6 × 1 supercells. The results demonstrate that the domain size of the catalyst has little impact on the overall adsorption trends of the intermediates (Table S2). Additionally, incorporating the implicit solvation model into our calculations revealed that the adsorption energy trends of the intermediates remained unchanged (Table S3). The above results indicate that the intermediates are adsorbed through a chemisorption process on FeN_4-embedded graphene, which would significantly influence the electronic properties of the systems.

Table 1. Calculated Shortest Distances (d) Between Intermediates and Fe Atom, Adsorption Energies (E_{ads}), and Charge Transfer (Q_T) from FeN_4-Embedded Graphene to the Atom Connected to the Substrate

	d (Å)	E_{ads} (eV)	Q_T (C or O)
*COOH	1.91	−2.25	+0.18 e
*OCHO	1.94	−2.36	+0.33 e
*CHO	1.89	−2.20	+0.10 e
*COH	1.70	−2.68	+0.11 e

Afterward, we analyzed the charge transfer through Bader charge analysis, as outlined in Table 1. The results reveal that a significant amount of charge was transferred from FeN_4-embedded graphene to intermediates, which agrees with the notable adsorption energies. It should be noted that there is no strictly proportional relationship between the number of transferred charges and adsorption energies because the formation of the atomic bond depends not only on the charge transfer between atoms but also on the sharing of electron pairs among atoms. In addition, the charge density differences were calculated as shown in Figure 2, in which the yellow and blue colors represent the electron-rich and deficient regions, respectively. It can be observed that the FeN_4-embedded graphene acts as an electron donator while the intermediates are electron acceptors. The apparent electron transfer confirms the significant interaction between FeN_4-embedded graphene and the intermediates. The charge redistribution plays a pivotal role in the adsorption process. It could induce orbital hybridization at the interface region, which grounds the modulation of electronic transport in the FeN_4-embedded graphene system.

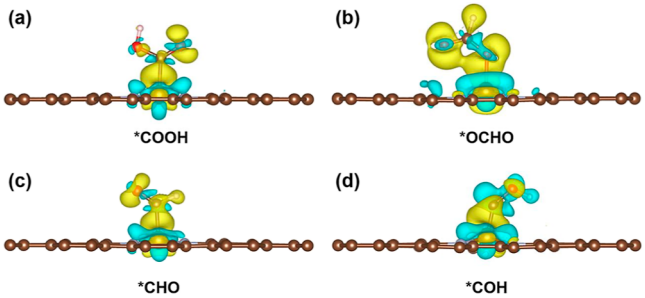

Figure 2. Charge density difference after the adsorption of (a) *COOH, (b) *OCHO, (c) *CHO, and (d) *COH on FeN_4-embedded graphene. Yellow and blue colors represent the charge accumulation and depletion regions, respectively. The isosurface value is set at 0.002 e/Å^3.

3.2. Electronic Properties of the Adsorbed Systems.

To understand the sensing mechanism, we investigated the electronic properties of FeN_4-embedded graphene and intermediate systems. We calculated the total DOS (TDOS) of FeN_4-embedded graphene with and without intermediates adsorption and the intermediates' projected DOS (PDOS). As presented in Figure S1, pristine FeN_4-embedded graphene is a semiconductor with a bandgap of about 0.4 eV. Upon the adsorption of intermediates on FeN_4-embedded graphene, the TDOS shifts to the right, resulting in modifications around the Fermi level. There is a significant difference in the DOS

https://doi.org/10.1021/acsomega.4c04465
ACS Omega 2024, 9, 32167−32174

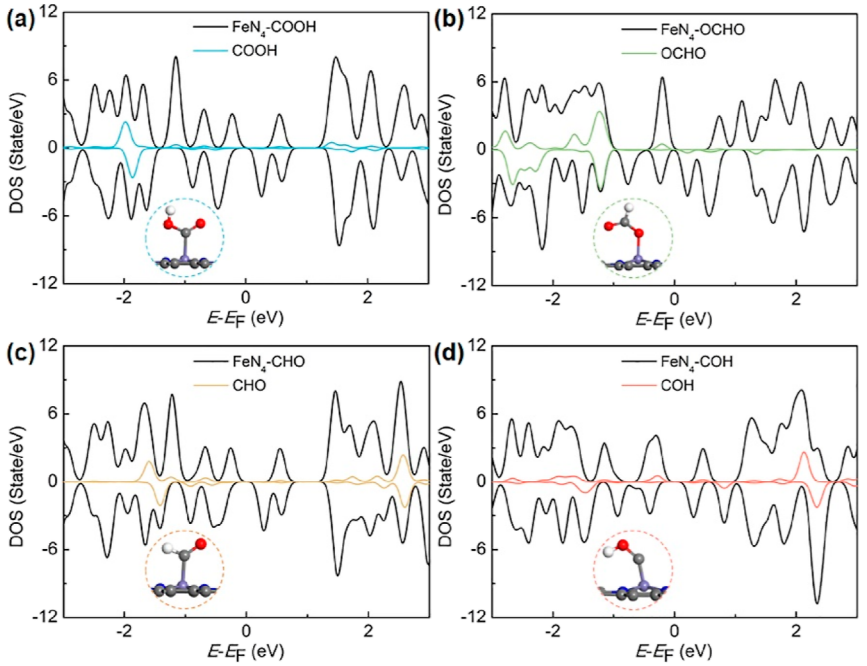

Figure 3. (a–d) Spin-polarized TDOS of the system with each intermediate adsorption (black lines) and the PDOS of the intermediates.

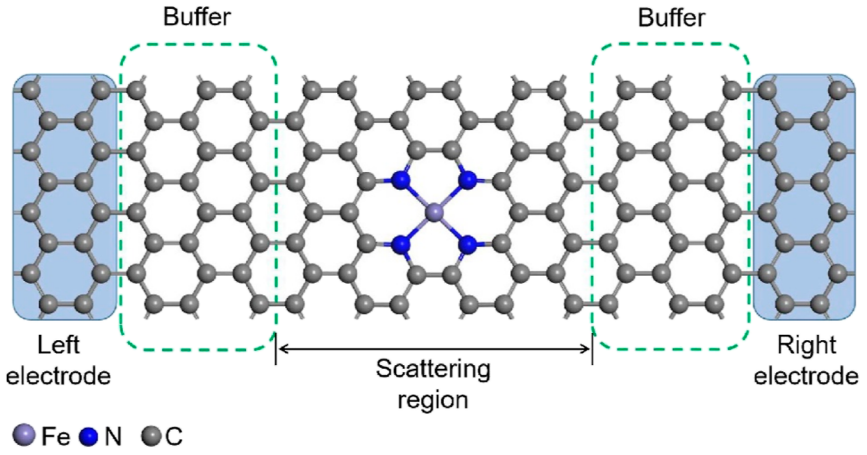

Figure 4. Schematic diagram of the dual-probe transport system for electron transport calculations, including the semi-infinite left and right electrodes (in shade) and the central device region. The current flows along the armchair direction.

between the intermediate's adsorbed systems because each intermediate interacts differently with the substrate depending on the molecular species and interactive characteristics.

For the first detection group, the results in Figure 3 reveal pronounced orbital hybridization near the Fermi level for *OCHO, while *COOH exhibits less obvious overlapping. For the second detection group, *COH contributes electronic states close to the Fermi level, while the states of *CHO are localized approximately 1.0 eV below and above the Fermi level. As demonstrated in Figure S2, the electronic states around the Fermi level primarily originate from the d orbital of the Fe atom and the p orbital of the connected C or O atom. The prominent electronic states of *OCHO and *COH around the Fermi level indicate their stronger interaction with the FeN_4-embedded graphene substrate, consistent with their higher adsorption energy. We also consider the effect of solvation on electronic properties, and the results show that the implicit solvation has little effect on the DOS (Figure S3).

3.3. Electronic Transport Properties. Our above results demonstrate that the charge transfer and new electronic states induced by the intermediate adsorption are expected to affect the resistivity of the host material, which renders FeN_4-embedded graphene a promising candidate for identifying CO_2 reduction intermediates and products. To assess its performance as an intermediate detection device for CO_2RR, we calculated the electronic transport properties of FeN_4-embedded graphene before and after intermediate adsorption using the non-equilibrium Green's function method. The chemisorption of the intermediate may introduce a scattering center that affects the charge transport. As shown in Figure 4, we devised a dual-probe system in which the device can be divided into three regions: semi-infinite left and right electrode regions and a central device region (including a central scattering region and buffer layer). The device configuration here is the same as in the electronic property calculations. The target intermediate adsorbed on the substrate is positioned in the central scattering region. Here, we only constructed the

https://doi.org/10.1021/acsomega.4c04465
ACS Omega 2024, 9, 32167−32174

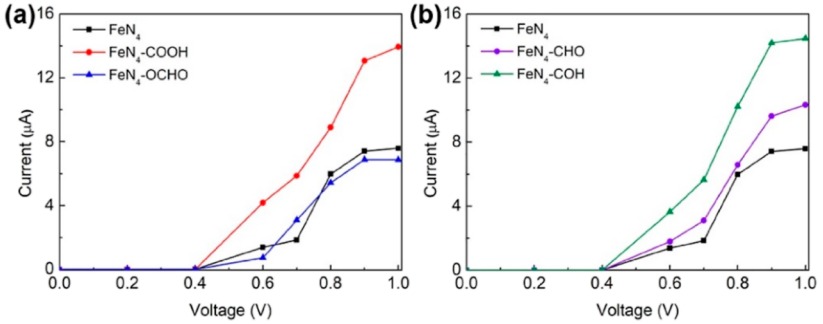

Figure 5. $I-V$ curves of the FeN_4-embedded graphene device before and after the adsorption of (a) *COOH and *OCHO and (b) *CHO and *COH intermediates, respectively.

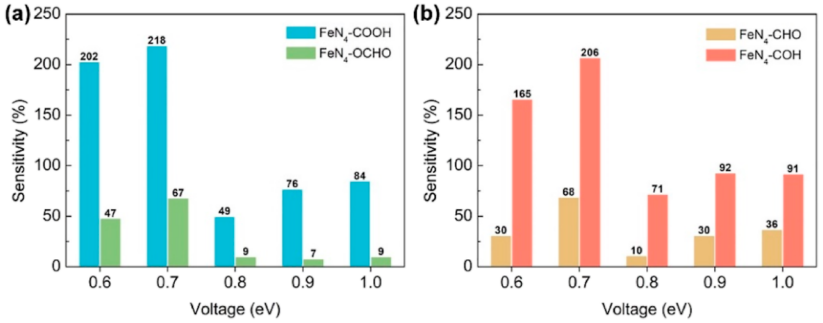

Figure 6. Sensitivity of the FeN_4-embedded graphene device for (a) *COOH and *OCHO and (b) *CHO and *COH intermediates at an applied bias voltage of 0.6−1.0 V, respectively.

transport model with current flowing along the armchair direction due to the isotropy of graphene. The calculated current−voltage ($I-V$) relationship is expected to give a substantial description of the resistivity variation.

The current−voltage curves for FeN_4-embedded graphene with and without intermediate adsorption are shown in Figure 5. When a bias voltage is applied, the Fermi level of the left electrode shifts upward relative to that of the right electrode. Consequently, the electrical current begins to flow only when the valence band maximum of the left electrode approaches the conduction band minimum of the right electrode. Therefore, no current is generated until the bias voltage exceeds 0.4 V, consistent with the bandgap of FeN_4-embedded graphene. As the bias voltage increases, the current in each system is enhanced to varying degrees. The difference in current of the device serves as the basis for identifying each intermediate. The $I-V$ plot reveals that all the intermediates can be distinctly identified within the 0.4−1.0 V bias window.

For the first detection group, the currents are in the following order at most bias voltages: *COOH > substrate > *OCHO. It is found that the current of the system with *COOH intermediate significantly deviates from that of the pristine substrate. In contrast the current of the system with *OCHO intermediate is close to it. At a bias voltage of 1.0 V, the value of current increases to 13.94 μA for *COOH while decreasing to 6.88 μA for *OCHO. Particularly, when the bias voltage is applied, the currents are increased after the adsorption of *COOH while decreasing with the adsorption of *OCHO compared to the pristine substrate. The current increase corresponds to the resistance reduction after the intermediate adsorption. However, *OCHO intermediate introduces a backscattering center that reduces available conductance channels, even though it exhibits a substantial adsorption property. The currents for the second detection group are in the following order: *COH > *CHO > substrate. When the bias voltage is increased to 1.0 V, the currents for *COH and *CHO are 14.47 and 10.33 μA, respectively. It can be seen that the current of the system with *COH adsorption exhibits notable changes compared with that of the pristine substrate, while the current of the *CHO adsorption system deviates slightly from the original current. The distinct current changes due to different adsorption indicate that FeN_4-embedded graphene exhibits high sensitivity and selectivity for detecting intermediates during the CO_2RR process.

As we know, sensitivity plays an important role in intermediate detection. The performance of a detection device depends on its sensitivity. The high sensitivity of a detector is the primary requirement for intermediate identification in CO_2RR. To evaluate the capability of FeN_4-embedded graphene for intermediate detection, we calculated the current sensitivity (S) by the following equation

$$S = \frac{|I - I_0|}{I_0} \times 100\% \tag{4}$$

where I_0 and I represent the currents before and after the intermediate adsorption on FeN_4-embedded graphene, respectively. Figure 6 shows a comparative bar chart of the percentage of detection sensitivity in FeN_4-embedded graphene. For the first detection group, the simulated device exhibits higher detection sensitivity toward *COOH intermediate while lower sensitivity toward *OCHO intermediate. The FeN_4-embedded graphene device can detect *COOH within the whole bias window. Remarkably, the current sensitivity values are 218% for *COOH and 67% for *OCHO at an applied bias of 0.7 V. For the second detection group, *COH yields higher current sensitivity values than *CHO and can be detected within the bias from 0.6 to 1.0 V.

https://doi.org/10.1021/acsomega.4c04465
ACS Omega 2024, 9, 32167−32174

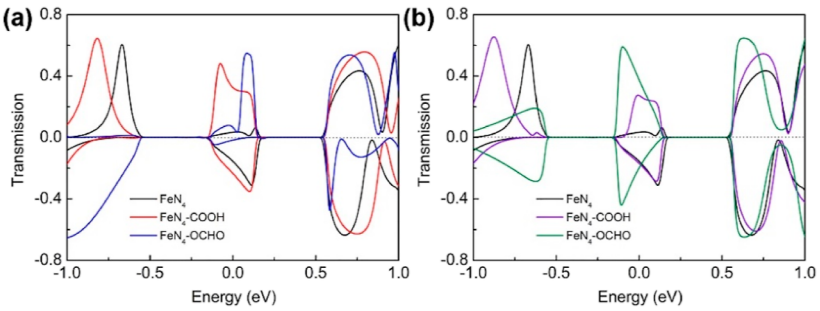

Figure 7. Spin-polarized transmission spectra of the FeN_4-embedded graphene device under the bias of 0.7 V before and after the adsorption of (a) *COOH and *OCHO and (b) *CHO and *COH intermediates, respectively.

Particularly, the current sensitivity values are 206% for *COH and 68% for *CHO at the bias of 0.7 V. Moreover, we found no proportional correlation between sensitivity and charge transfer or adsorption energy, suggesting that the comprehensive influence of different intermediates on the substrate ultimately determines the sensitivity. Based on the above results, we believe that the FeN_4-embedded graphene device can distinguish intermediates with high sensitivity and selectivity during the CO_2RR process.

3.4. Electronic Transmission Spectra. To investigate the underlying mechanism of transport property difference caused by intermediates, we computed the equilibrium transmission coefficients of FeN_4-embedded graphene before and after intermediates adsorption. The electronic transmission coefficient reflects the probability of electrons transferring from the left to the right electrode through the central scattering region. Typically, wide and high transmission peaks around the Fermi level signify that sufficient conductance channels are available for electron transport, while the sharp peaks correspond to a reduction in conductance channels and lead to decreased current. Figure 7 shows the spin-polarized transmission spectra of the systems before and after intermediate adsorption under the bias of 0.7 V. It can be seen that the spin-up transmission coefficient of the *COOH adsorbed system around the Fermi level increases sharply relative to the pure system and the spin-down transmission coefficient also increases, leading to extremely high sensitivity. For the *OCHO adsorbed system, the spin-up transmission coefficient increases significantly while the spin-down transmission coefficient is reduced, resulting in considerable sensitivity. For the second detection group, it shows that the *COH adsorption causes a pronounced increase of transmission in both spin-up and spin-down channels, yielding higher current and ultra-high sensitivity. The *CHO adsorption causes an increase in spin-up transmission, while the spin-down transmission spectrum almost coincides with that of the pristine substrate, contributing to apparent sensitivity. Additional electron transmission spectra under other bias values are shown in Figures S4 and S5. The variation of transmission coefficient is also consistent with the change amplitude of the spin-polarized currents shown in Figure S6. Within the bias window, we can find the spin-polarized currents of *COOH and *COH adsorbed systems are significantly higher than that of the pristine substrate in the spin-up channel but only slightly higher in the spin-down channel, which leads to invariably high sensitivity for *COOH and *COH detection. With the adsorption of *OCHO and *CHO, the spin-up currents increase compared to the pristine substrate. In contrast, the spin-down currents decrease, resulting in high selectivity with other intermediates but high sensitivity only at specific biases. Overall, the distinct sensitivity values due to the intermediate adsorption confirm the high selectivity of the FeN_4-embedded graphene device at all biases and the ultrahigh sensitivity at the bias of 0.7 V.

4. CONCLUSION

In summary, we explored the potential of FeN_4-embedded graphene for intermediate detection during the CO_2RR process based on the combination of DFT and NEGF approaches. The first protonated intermediates (*COOH and *OCHO) are taken as the first detection group, and the subsequent protonated intermediates (*CHO and *COH) are taken as the second detection group. It is found that the intermediates are chemisorbed on the surface with high adsorption energy and appropriate charge transfer. The effect of intermediate adsorption on the electronic properties of the system was investigated to reveal the interaction between intermediate and FeN_4-embedded graphene, which established the substrate material as an ideal candidate for intermediate detection devices. Furthermore, the electronic transport properties were calculated to evaluate the performance of the FeN_4-embedded graphene device for intermediate detection. The $I-V$ curves and transmission spectra under applied biases demonstrated a distinct difference in each detection group. The sensitivity analysis revealed that the FeN_4-embedded graphene exhibits significantly higher sensitivity to *COOH and *COH than to *OCHO and *CHO within the bias window. Notably, all intermediates show high sensitivity and selectivity at the bias of 0.7 V. We have also noted no proportional relationship between sensitivity and charge transfer or adsorption energy, demonstrating that the different types of intermediates ultimately determine the sensitivity. Overall, this work identifies the feasibility of FeN_4-embedded graphene for individual intermediate detection and provides a practical strategy for elucidating the mechanisms of CO_2RR.

■ ASSOCIATED CONTENT

Supporting Information

The Supporting Information is available free of charge at https://pubs.acs.org/doi/10.1021/acsomega.4c04465.

TDOS of the pristine substrate and the intermediate adsorbed systems, PDOS of substrate-attached atoms and Fe atom in intermediate adsorbed systems with and without the implicit solvation model, spin-polarized $I-V$ curves, spin-polarized transmission spectra, the adsorption energy of the intermediates calculated by PBE + U, the adsorption energy of the intermediates calculated by

https://doi.org/10.1021/acsomega.4c04465
ACS Omega 2024, 9, 32167−32174

using 5 × 5 × 1 and 6 × 6 × 1 supercells, and the adsorption energy of intermediates calculated by using an implicit solvation model (PDF)

AUTHOR INFORMATION

Corresponding Authors

Xiaocheng Zhou − *Jiangsu Key Laboratory of New Power Batteries, Jiangsu Collaborative Innovation Centre of Biomedical Functional Materials, School of Chemistry and Materials Science, Nanjing Normal University, Nanjing 210023, China*; Email: xczhou@njnu.edu.cn

Yafei Li − *Jiangsu Key Laboratory of New Power Batteries, Jiangsu Collaborative Innovation Centre of Biomedical Functional Materials, School of Chemistry and Materials Science, Nanjing Normal University, Nanjing 210023, China*; orcid.org/0000-0003-2587-820X; Email: liyafei@njnu.edu.cn

Authors

Yuqi Cai − *Jiangsu Key Laboratory of New Power Batteries, Jiangsu Collaborative Innovation Centre of Biomedical Functional Materials, School of Chemistry and Materials Science, Nanjing Normal University, Nanjing 210023, China*

Yu Wang − *Jiangsu Key Laboratory of New Power Batteries, Jiangsu Collaborative Innovation Centre of Biomedical Functional Materials, School of Chemistry and Materials Science, Nanjing Normal University, Nanjing 210023, China*; orcid.org/0000-0002-8833-9564

Complete contact information is available at: https://pubs.acs.org/10.1021/acsomega.4c04465

Notes

The authors declare no competing financial interest.

ACKNOWLEDGMENTS

The authors are grateful for funding support from the National Key R&D Program of China (2019YFA0308000), the Natural Science Foundation of China (no. 22173048, no. 12202209), Natural Science Foundation of Jiangsu Province (BK20220379), and the Priority Academic Program Development of Jiangsu Higher Education Institutions. We also gratefully acknowledge HZWTECH for providing computation facilities.

REFERENCES

(1) Olah, G. A.; Prakash, G. K. S.; Goeppert, A. Anthropogenic Chemical Carbon Cycle for a Sustainable Future. *J. Am. Chem. Soc.* **2011**, *133* (33), 12881−12898.

(2) Goldthau, A. The G20 Must Govern the Shift to Low-Carbon Energy. *Nature* **2017**, *546* (7657), 203−205.

(3) Xu, S.; Carter, E. A. Theoretical Insights into Heterogeneous (Photo)Electrochemical CO_2 Reduction. *Chem. Rev.* **2019**, *119* (11), 6631−6669.

(4) Nitopi, S.; Bertheussen, E.; Scott, S. B.; Liu, X.; Engstfeld, A. K.; Horch, S.; Seger, B.; Stephens, I. E. L.; Chan, K.; Hahn, C.; Nørskov, J. K.; Jaramillo, T. F.; Chorkendorff, I. Progress and Perspectives of Electrochemical CO_2 Reduction on Copper in Aqueous Electrolyte. *Chem. Rev.* **2019**, *119* (12), 7610−7672.

(5) Kibria, M. G.; Edwards, J. P.; Gabardo, C. M.; Dinh, C.-T.; Seifitokaldani, A.; Sinton, D.; Sargent, E. H. Electrochemical CO_2 Reduction into Chemical Feedstocks: From Mechanistic Electrocatalysis Models to System Design. *Adv. Mater.* **2019**, *31* (31), 1807166.

(6) Xu, F.; Wang, X.; Liu, X.; Li, C.; Fan, G.; Xu, H. Computational Screening of TMN_4 Based Graphene-Like BC_6N for CO_2 Electroreduction to C1 Hydrocarbon Products. *Mol. Catal.* **2022**, *530*, 112571.

(7) Wang, Y.; Cheng, L.; Ge, W.; Zhu, Y.; Zhang, J.; Chen, R.; Zhang, L.; Li, Y.; Li, C. Effect of Charge on Carbon Support on the Catalytic Activity of Cu_2O toward CO_2 Reduction to C2 Products. *ACS Appl. Mater. Interfaces* **2023**, *15* (19), 23306−23315.

(8) Li, X.; Wang, S.; Li, L.; Sun, Y.; Xie, Y. Progress and Perspective for In Situ Studies of CO_2 Reduction. *J. Am. Chem. Soc.* **2020**, *142* (21), 9567−9581.

(9) Deng, B.; Huang, M.; Zhao, X.; Mou, S.; Dong, F. Interfacial Electrolyte Effects on Electrocatalytic CO_2 Reduction. *ACS Catal.* **2022**, *12* (1), 331−362.

(10) Lum, Y.; Ager, J. W. Stability of Residual Oxides in Oxide-Derived Copper Catalysts for Electrochemical CO_2 Reduction Investigated with ^{18}O Labeling. *Angew. Chem., Int. Ed.* **2018**, *57* (2), 551−554.

(11) Zu, X.; Li, X.; Liu, W.; Sun, Y.; Xu, J.; Yao, T.; Yan, W.; Gao, S.; Wang, C.; Wei, S.; Xie, Y. Efficient and Robust Carbon Dioxide Electroreduction Enabled by Atomically Dispersed $Sn^{\delta+}$ Sites. *Adv. Mater.* **2019**, *31* (15), 1808135.

(12) Ahn, S. M.; Suk, J.; Kim, D. Y.; Kang, Y.; Kim, H. K.; Kim, D. W. High-Performance Lithium-Oxygen Battery Electrolyte Derived from Optimum Combination of Solvent and Lithium Salt. *Adv. Sci.* **2017**, *4* (10), 1700235.

(13) Todoroki, N.; Tei, H.; Tsurumaki, H.; Miyakawa, T.; Inoue, T.; Wadayama, T. Surface Atomic Arrangement Dependence of Electrochemical CO_2 Reduction on Gold: Online Electrochemical Mass Spectrometric Study on Low-Index Au(hkl) Surfaces. *ACS Catal.* **2019**, *9* (2), 1383−1388.

(14) Clark, E. L.; Bell, A. T. Direct Observation of the Local Reaction Environment during the Electrochemical Reduction of CO_2. *J. Am. Chem. Soc.* **2018**, *140* (22), 7012−7020.

(15) Pandey, M.; Pandey, C.; Ahuja, R.; Kumar, R. Straining Techniques for Strain Engineering of 2D Materials towards Flexible Straintronic Applications. *Nano Energy* **2023**, *109*, 108278.

(16) Wu, Z.; Qi, J.; Wang, W.; Zeng, Z.; He, Q. Emerging Elemental Two-Dimensional Materials for Energy Applications. *J. Mater. Chem. A* **2021**, *9* (35), 18793−18817.

(17) Mehdi Pour, M.; Lashkov, A.; Radocea, A.; Liu, X.; Sun, T.; Lipatov, A.; Korlacki, R. A.; Shekhirev, M.; Aluru, N. R.; Lyding, J. W.; Sysoev, V.; Sinitskii, A. Laterally Extended Atomically Precise Graphene Nanoribbons with Improved Electrical Conductivity for Efficient Gas Sensing. *Nat. Commun.* **2017**, *8* (1), 820.

(18) Szczęśniak, B.; Choma, J.; Jaroniec, M. Gas Adsorption Properties of Graphene-Based Materials. *Adv. Colloid Interface Sci.* **2017**, *243*, 46−59.

(19) de Souza, F. A. L.; Amorim, R. G.; Prasongkit, J.; Scopel, W. L.; Scheicher, R. H.; Rocha, A. R. Topological Line Defects in Graphene for Applications in Gas Sensing. *Carbon* **2018**, *129*, 803−808.

(20) Liu, G.; Chen, T.; Dong, X.; Huang, L.; Xu, Z.; Xiao, X. High Gas Sensing Performance of Inorganic and Organic Molecule Sensing Devices Based on the BC_3N_2 Monolayer. *Phys. Chem. Chem. Phys.* **2022**, *24* (38), 23769−23778.

(21) Sajjad, M.; Morell, G.; Feng, P. Advance in Novel Boron Nitride Nanosheets to Nanoelectronic Device Applications. *ACS Appl. Mater. Interfaces* **2013**, *5* (11), 5051−5056.

(22) Ko, K. Y.; Lee, S.; Park, K.; Kim, Y.; Woo, W. J.; Kim, D.; Song, J.-G.; Park, J.; Kim, J. H.; Lee, Z.; Kim, H. High-Performance Gas Sensor Using a Large-Area $WS_{2x}Se_{2-2x}$ Alloy for Low-Power Operation Wearable Applications. *ACS Appl. Mater. Interfaces* **2018**, *10* (40), 34163−34171.

(23) Perkins, F. K.; Friedman, A. L.; Cobas, E.; Campbell, P. M.; Jernigan, G. G.; Jonker, B. T. Chemical Vapor Sensing with Monolayer MoS_2. *Nano Lett.* **2013**, *13* (2), 668−673.

(24) Naqvi, S. R.; Shukla, V.; Jena, N. K.; Luo, W.; Ahuja, R. Exploring Two-Dimensional M_2NS_2 (M = Ti, V) MXenes Based Gas Sensors for Air Pollutants. *Appl. Mater. Today* **2020**, *19*, 100574.

(25) Kou, L.; Frauenheim, T.; Chen, C. Phosphorene as a Superior Gas Sensor: Selective Adsorption and Distinct *I-V* Response. *J. Phys. Chem. Lett.* **2014**, *5* (15), 2675−2681.
(26) Tsai, H.-S.; Wang, Y.; Liu, C.; Wang, T.; Huo, M. The Elemental 2D Materials beyond Graphene Potentially Used as Hazardous Gas Sensors for Environmental Protection. *J. Hazard. Mater.* **2022**, *423*, 127148.
(27) Cho, B.; Yoon, J.; Hahm, M. G.; Kim, D.-H.; Kim, A. R.; Kahng, Y. H.; Park, S.-W.; Lee, Y.-J.; Park, S.-G.; Kwon, J.-D.; Kim, C. S.; Song, M.; Jeong, Y.; Nam, K.-S.; Ko, H. C. Graphene-Based Gas Sensor: Metal Decoration Effect and Application to a Flexible Device. *J. Mater. Chem. C* **2014**, *2* (27), 5280−5285.
(28) Li, X.; Bi, W.; Chen, M.; Sun, Y.; Ju, H.; Yan, W.; Zhu, J.; Wu, X.; Chu, W.; Wu, C.; Xie, Y. Exclusive Ni-N_4 Sites Realize Near-Unity CO Selectivity for Electrochemical CO_2 Reduction. *J. Am. Chem. Soc.* **2017**, *139* (42), 14889−14892.
(29) Wang, J.; Li, Z.; Wu, Y.; Li, Y. Fabrication of Single-Atom Catalysts with Precise Structure and High Metal Loading. *Adv. Mater.* **2018**, *30* (48), 1801649.
(30) Lu, Z.; Yang, M.; Ma, D.; Lv, P.; Li, S.; Yang, Z. CO Oxidation on Mn-N_4 Porphyrin-Like Carbon Nanotube: A DFT-D Study. *Appl. Surf. Sci.* **2017**, *426*, 1232−1240.
(31) Lu, S.; Lou, F.; Zhao, Y.; Yu, Z. Regulating the Coordination Environment of Single-Atom Catalysts for Electrocatalytic CO_2 Reduction. *J. Colloid Interface Sci.* **2023**, *646*, 301−310.
(32) Li, X.; Xi, S.; Sun, L.; Dou, S.; Huang, Z.; Su, T.; Wang, X. Isolated FeN_4 Sites for Efficient Electrocatalytic CO_2 Reduction. *Adv. Sci.* **2020**, *7* (17), 2001545.
(33) Kresse, G.; Furthmüller, J. Efficient Iterative Schemes for Ab Initio Total-Energy Calculations Using a Plane-Wave Basis Set. *Phys. Rev. B: Condens. Matter Mater. Phys.* **1996**, *54* (16), 11169−11186.
(34) Perdew, J. P.; Burke, K.; Ernzerhof, M. Generalized Gradient Approximation Made Simple. *Phys. Rev. Lett.* **1996**, *77* (18), 3865−3868.
(35) Mathew, K.; Kolluru, V. S. C.; Mula, S.; Steinmann, S. N.; Hennig, R. G. Implicit Self-Consistent Electrolyte Model in Plane-Wave Density-Functional Theory. *J. Chem. Phys.* **2019**, *151* (23), 234101.
(36) Mathew, K.; Sundararaman, R.; Letchworth-Weaver, K.; Arias, T. A.; Hennig, R. G. Implicit Solvation Model for Density-Functional Study of Nanocrystal Surfaces and Reaction Pathways. *J. Chem. Phys.* **2014**, *140* (8), 084106.
(37) Taylor, J.; Guo, H.; Wang, J. Ab Initio Modeling of Quantum Transport Properties of Molecular Electronic Devices. *Phys. Rev. B: Condens. Matter Mater. Phys.* **2001**, *63* (24), 245407.
(38) Büttiker, M.; Imry, Y.; Landauer, R.; Pinhas, S. Generalized Many-Channel Conductance Formula with Application to Small Rings. *Phys. Rev. B: Condens. Matter Mater. Phys.* **1985**, *31* (10), 6207−6215.
(39) Panigrahi, P.; Panda, P. K.; Pal, Y.; Bae, H.; Lee, H.; Ahuja, R.; Hussain, T. Two-Dimensional Bismuthene Nanosheets for Selective Detection of Toxic Gases. *ACS Appl. Nano Mater.* **2022**, *5* (2), 2984−2993.
(40) Prasongkit, J.; de Freitas Martins, E.; de Souza, F. A. L.; Scopel, W. L.; Amorim, R. G.; Amornkitbamrung, V.; Rocha, A. R.; Scheicher, R. H. Topological Line Defects around Graphene Nanopores for DNA Sequencing. *J. Phys. Chem. C* **2018**, *122* (13), 7094−7099.
(41) Nematollahi, P.; Barbiellini, B.; Bansil, A.; Lamoen, D.; Jia, Q.; Mukerjee, S.; Neyts, E. C. Identification of a Robust and Durable FeN_4C_x Catalyst for ORR in PEM Fuel Cells and the Role of the Fifth Ligand. *ACS Catal.* **2022**, *12* (13), 7541−7549.
(42) Yang, N.; Peng, L.; Li, L.; Li, J.; Liao, Q.; Shao, M.; Wei, Z. Theoretically Probing the Possible Degradation Mechanisms of an FeNC Catalyst during the Oxygen Reduction Reaction. *Chem. Sci.* **2021**, *12* (37), 12476−12484.

https://doi.org/10.1021/acsomega.4c04465
ACS Omega 2024, 9, 32167−32174